HHS Public Access

Author manuscript

J Phys Chem B. Author manuscript; available in PMC 2023 February 17.

Published in final edited form as:

J Phys Chem B. 2022 February 17; 126(6): 1202–1211. doi:10.1021/acs.jpcb.1c10131.

The N-Terminal Domain of Aβ_{40}-Amyloid Fibril: The MOMD Perspective of its Dynamic Structure from NMR Lineshape Analysis

Eva Meirovitch,

The Mina and Everard Goodman Faculty of Life Sciences, Bar-Ilan University, Ramat-Gan 52900, Israel;

Zhichun Liang,

Baker Laboratory of Chemistry and Chemical Biology, Cornell University, Ithaca, New York 14853-1301, United States

Jack H. Freed

Baker Laboratory of Chemistry and Chemical Biology, Cornell University, Ithaca, New York 14853-1301, United States;

Abstract

We have developed the stochastic microscopic-order-macroscopic-disorder (MOMD) approach for elucidating dynamic structures in the solid-state from ^{2}H NMR lineshapes. In MOMD, the probe experiences an effective/collective motional mode. The latter is described by a potential, u, which represents the local spatial-restrictions, a local-motional diffusion tensor, $\boldsymbol{R}$, and key features of local geometry. Previously we applied MOMD to the well-structured core domain of the 3-fold-symmetric twisted polymorph of the Aβ_{40}-amyloid fibril. Here, we apply it to the N-terminal domain of this fibril. We find that the dynamic structures of the two domains are largely similar but differ in the magnitude and complexity of the key physical parameters. This interpretation differs from previous multisimple-mode (MSM) interpretations of the same experimental data. MSM used for the two domains different combinations of simple motional modes taken to be independent. For the core domain, MOMD and MSM disagree on the character of the dynamic structure. For the N-terminal domain, they even disagree on whether this chain segment is structurally ordered (MOMD finds that it is), and whether it undergoes a phase transition at 260 K where bulklike water located in the fibril matrix freezes (MOMD finds that it does not). These are major differences associated with an important system. While the MOMD description

Corresponding Authors: **Eva Meirovitch** – The Mina and Everard Goodman Faculty of Life Sciences, Bar-Ilan University, Ramat-Gan 52900, Israel; Phone: 972-3-531-8049; eva.meirovitch@biu.ac.il, **Jack H. Freed** – Baker Laboratory of Chemistry and Chemical Biology, Cornell University, Ithaca, New York 14853-1301, United States; Phone: 607-255-3647; jhf3@cornell.edu.

Supporting Information

The Supporting Information is available free of charge at https://pubs.acs.org/doi/10.1021/acs.jpcb.1c10131.

Schematic of the τ-histidine molecule; experimental ^{2}H lineshapes yielded by the C$^{\alpha}$–C$^{\beta}$D$_3$ probe of residue A2 and the (N-ring)–CD$_3$ probe of residue τ-H6 at various temperatures; experimental ^{2}H lineshapes yielded by the C$^{\beta}$–phenyl-d_5 probe of residue F4 and the C$^{\alpha}$–D probe of residue G9 at various temperatures; experimental ^{2}H lineshapes yielded by the C$^{\alpha}$–C$^{\beta}$D$_3$ probe of residue A2 and the C$^{\beta}$–phenyl-d_5 probe of residue F4 at various temperatures (PDF)

Complete contact information is available at: https://pubs.acs.org/10.1021/acs.jpcb.1c10131

The authors declare no competing financial interest.

is a physically sound one, there are drawbacks in the MSM descriptions. The results obtained in this study promote our understanding of the dynamic structure of protein aggregates. Thus, they contribute to the effort to pharmacologically control neurodegenerative disorders believed to be caused by such aggregates.

Graphical Abstract

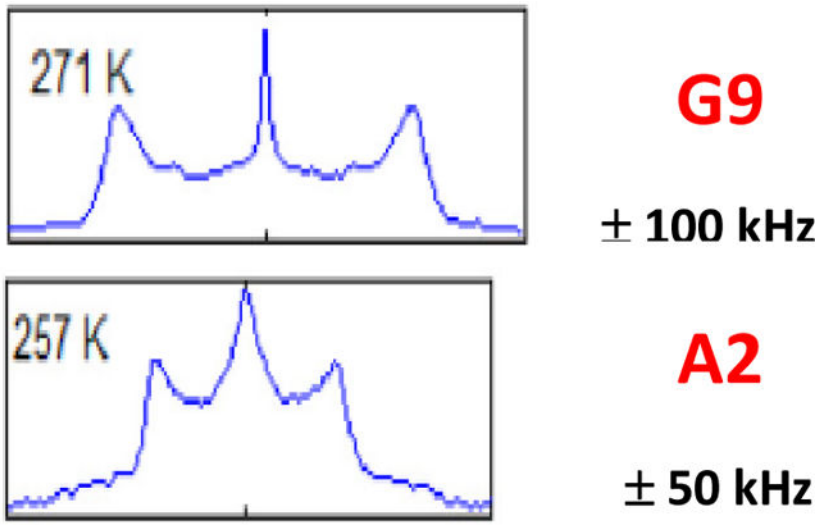

1. INTRODUCTION

Beta-amyloids are relatively small peptides (36–45 residues) produced by endoproteolitic cleavage of the amyloid precursor protein, which forms fibrils. The Aβ_{40}-amyloid, Aβ_{42}-amyloid fibrils, and associated aggregates are the main molecular manifestation of Alzheimer's disease (AD).[1–4] To aid in developing effective preventive and therapeutic agents for this devastating illness, it is helpful to better understand the dynamic structure of Aβ-amyloid systems, typically available in the form of polycrystalline morphologies.[5–10]

In this context, the analysis of ^{2}H NMR lineshapes in terms of structural dynamics is a particularly powerful method.[11–16] Let us focus on the CD_3 and phenyl-d_5 moieties as physical probes. There exists two different approaches for analyzing the respective ^{2}H spectra. They include the multisimple-mode (MSM) method where several simple motions are combined (e.g., ref 15), and the stochastic microscopic-order-macroscopic-disorder (MOMD) approach which provides an effective/collective motional mode.[16] Both MSM (refs 17 and 18) and MOMD (refs 19 and 20) were applied previously to the core domain of the three-fold-symmetric twisted polymorph of the Aβ_{40}-amyloid fibril (residues 17–40), known to be well-structured (we use below the abbreviation "Aβ_{40}-amyloid fibril"). References 17 and 19 utilized CD_3 probes whereas refs 18 and 20 used phenyl-d_5 probes. MSM was also applied to the N-terminal domain of this fibril (residues 1–16) suggesting, among others, that this domain is structurally disordered.[21]

MSM and MOMD have been discussed in previous publications.[16–20,22,23] The benefit of MSM is intuitive conceptualization of several simple motions. A drawback is the fact that

mode-independence is assumed without accounting for any collective interactions among these modes, hence limiting the relevance of the results provided by the overall model.

MOMD is physically well-defined; based on established principles for treating restricted motions[24–29] it solves the appropriate Stochastic Liouville Equation (SLE).[24–27] An effective/collective motional mode is used to describe the structural dynamics. This is a more phenomenological approach, more consistent with the limited resolution to the dynamics obtainable from the NMR spectrum. The pertinent physical quantities are treated with due consideration to their three-dimensional tensorial properties. The motion is expressed by a diffusion tensor, $\boldsymbol{R}$; the spatial restrictions by a potential, u, expanded in the basis set of the real Wigner functions, $D^{L}_{0|K|}$ (i.e., the real generalized spherical harmonics); and the local geometry is represented by the relative orientation of the tensors of the motional model and the NMR tensors.[16]

In applying MOMD to the core domain of the Aβ_{40}-amyloid fibril, we found that it is sufficient to expand the local potential as $u = -c_0^2 D_{0,0}^2 - c_2^2\left(D_{0,2}^2 + D_{0,-2}^2\right)$, to take the local diffusion tensor, $\boldsymbol{R}$, to be axially symmetric, and to describe the local geometry by a single polar angle, β_{MQ}.[19,20] This description, where the parameters c_0^2, c_2^2, $R_{\parallel}$, $R_{\perp}$, and β_{MQ} are determined from the analysis of the spectrum, is made possible by treating consistently all of the probes.

CD_3 probes of valine, leucine, and methionine residues were studied in the 245-to-310 K temperature range.[19] The ^{2}H spectra of valine and leucine evolve gradually as a function of temperature, that is, no abrupt change is observed. On the other hand, the ^{2}H spectrum of methionine 35 (M35) changes abruptly at 260 K, where bulklike water in the fibril matrix freezes. This event causes a change in the symmetry of the potential, u. M35 is the only residue residing at the fibril interface, as does tightly peptide-bound water. It was suggested that the impact of water-freezing is transmitted to the fibril structure through interaction with tightly peptide-bound water, in this case of the M35 methyl moiety.[19]

MOMD analysis of the phenyl-d_5 probes was also carried out using the local potential noted above and taking the diffusion tensor to be axially symmetric. This made possible useful comparisons among the dynamic structures of the Aβ_{40}-amyloid fibril, the protofibril of the D23N mutant, and the globular protein Chicken Villin Headpiece Subdomain.[20]

The MSM-based interpretation of the CD_3 spectra of the core domain is as follows.[17] The C–CD_3 bonds of valine and leucine execute rotameric exchange among three and four sites, respectively, involving different sets of side-chain dihedral angles and different patterns of population distribution. The exchange rates are determined by imposing linearity on the inverse temperature-dependence of their natural logarithms. Independently the C–CD_3 bonds execute small-angle jumps of adjustable rate along arcs of adjustable length. The sudden change in the M35 spectrum at 260 K is ascribed to methionine featuring the valine model below, and the leucine model above, this temperature.

The phenyl-d_5 probes have been analyzed with a completely different MSM model.[18] Exchange among four symmetry-related sites is postulated. It is maintained that slow flips

take place between the distant sites 1–3 and 2–4 while fast flips take place between the adjacent sites 1–2 and 3–4; this is difficult to reconcile. The activation energies for these motions are ascribed different types of distribution with mean values, widths, and associated pre-exponential Arrhenius factors allowed to vary in the data-fitting process. The activation energies are considered to represent ordering potentials. This is quite difficult to rationalize.

The MSM picture of N-terminal domain dynamics is in our minds even more problematic.[21] Residues A2, τ-H6 (a schematic thereof is depicted in Figure S1), F4, G9, and V12 have been labeled at their methyl or phenyl side chain positions. All of the ^{2}H spectra exhibit a peaklike feature at $\omega = 0$. The latter is interpreted to represent a "free" state, that is, a situation in which the N-terminal domain executes unrestricted isotropic rotational reorientation. This is inconsistent with the notion that motion in the solid-state is invariably restricted in its nature. In a subsequent article, the same authors maintain that even two different "free" states exist.[30] The "free" state coexists with a "bound" state. The population of the "free" state increases with increasing temperature. At 310 K, residues A2 and τ-H6 move exclusively "freely", while residues F4, G9, and V12 participate in both "free" and "bound" motion. In many cases the "free" motion slows down with increasing temperature. These situations are difficult to reconcile.

A peaklike feature at $\omega = 0$ does not necessarily represent isotropic overall motion. It could represent an orientation (not sampled) associated with a given restricted dynamic process. There are such examples in the early literature.[11,31] As shown below, MOMD analysis identifies such motions occurring in the N-terminal domain. How this is accomplished, and what the new insights gained are, are delineated in the following sections. Thus, together with the previous MOMD analysis of the core domain,[19,20] this study offers a physically well-defined description of the dynamic structure for the entire Aβ_{40}-amyloid fibril.

The theoretical background is summarized in Section 2. Results and discussion are presented in Section 3 and our conclusions appear in Section 4.

2. THEORETICAL BACKGROUND

The MOMD theory as applied to ^{2}H NMR has been described previously.[16,19,20,22,23,32] For convenience, it is outlined below. Figure 1 shows the MOMD frame scheme for C–D as probe. L is the space-fixed laboratory frame, and C is the local director frame fixed in the molecule, given in this case by the equilibrium orientation of the C–D bond. M denotes the principal axes system (PAS) of the local ordering tensor, **S**, defined in terms of the restricting/ordering potential, u. For simplicity, the PAS of the local ordering tensor and the PAS of the local diffusion tensor, $\boldsymbol{R}$, are taken as the same. Q denotes the PAS of the quadrupolar tensor. The M and Q frames are fixed in the probe.[16]

The Euler angles Ω_{CM} are time-dependent due to the molecular motions. The Euler angles $\Omega_{MQ} = (\alpha_{MQ}, \beta_{MQ}, \gamma_{MQ})$ are time-independent. Given that here the Q frame is axially symmetric, one has $\gamma_{MQ} = 0$. For convenience, the angle α_{MQ} is set equal to zero. Thus, the orientation of Z_M (main ordering/diffusion axis) relative to Z_Q (the principal axis of the

quadrupolar tensor pointing along the C–D bond) is given by the polar angle, β_{MQ}, called "diffusion tilt".

The stochastic Liouville equation (SLE) for a particle diffusing in an anisotropic medium, for the special case where the director is parallel to the applied magnetic field ($\Omega_{LC}= 0$), is given by[24]

$$\left(\frac{\partial}{\partial t}\right)\rho(\Omega,t) = \left[-iH(\Omega)^X - \Gamma_\Omega\right]\rho(\Omega,t), \quad \text{with } \Gamma_\Omega P_0(\Omega) = 0 \tag{1}$$

The Euler angles $\Omega \rightarrow (\alpha, \beta, \gamma)$ are the same as Ω_{CM} in the notation above. Γ_Ω is a Markovian operator for the rotational reorientation of the spin-bearing moiety (the physical probe, in this case the C–D bond). $\mathscr{H}(\Omega)^X$ is the quantum Liouville operator, that is, the commutator superoperator defined in terms of $\mathscr{H}(\Omega)$, the probe spin Hamiltonian describing the magnetic interactions. $P(\Omega, t)$ is the probability of finding Ω at the particular state at time, t, and $P_0(\Omega)$ is the unique equilibrium probability distribution of $P(\Omega, t)$ defined by $\Gamma_\Omega P(\Omega, t) = 0$. $\rho(\Omega, t)$ is the density matrix operator describing the joint evolution of the quantum spin degrees of freedom and the classical motion coordinates, Ω.

A simple form of the diffusion operator, $\Gamma_{\Omega,}$ is[24]

$$-\Gamma_\Omega = R\nabla^2_\Omega P(\Omega,t) - (R/kT)(\sin\beta)^{-1}\partial/\partial\beta[\sin\beta \mathrm{TP}(\Omega,t)] \tag{2}$$

where R is the isotropic rotational diffusion rate constant, ∇^2_Ω is the rotational diffusion operator in the Euler angles, Ω, and **T** is the restoring torque. The latter is equal to $\partial u/\partial\beta$ for an axial restoring potential, for example, $u \cong -3/2\, c_0^2(\cos\beta)^2$ (u is given in units of kT; i.e., it is dimensionless). The expression of Γ_Ω for rhombic diffusion tensor and rhombic potential is given in ref 25. Reference 26 comprises the extension of the theory to arbitrary Ω_{LC}.

In polycrystalline morphologies discussed herein, there is no "macroscopic order" aligning the molecules. Therefore, one has to calculate ^{2}H NMR spectra for a large enough number of director orientations (i.e., Ω_{LC} values), and sum the individual lineshapes according to random distribution; this completes the MOMD model.[16,27]

In this study, we are using an axial diffusion tensor, $\boldsymbol{R}$, associated in the absence of a restricting potential with three decay rates, $\tau_K^{-1} = 6R_\perp + K^2(R_\parallel - R_\perp)$ where $K = 0, 1, 2$ (K is the order of the rank-2 diffusion tensor). $R_\parallel$ and $R_\perp$ are the principal values of $\boldsymbol{R}$; one may also choose to define $\tau_\parallel = 1/(6R_\parallel)$ and $\tau_\perp = 1/(6R_\perp)$.[25]

For a uniaxial local director, one may expand the potential in the complete basis set of the Wigner rotation matrix elements with M = 0, $D^L_{0,K}(\Omega_{CM})$. One has[25–27]

$$u(\Omega_{CM}) = \frac{U(\Omega_{CM})}{kT} = -\sum_{L=1}^{\infty}\sum_{K=-L}^{+L} c_K^L D^L_{0,K}(\Omega_{CM}) \tag{3}$$

with $u(\Omega_{CM})$ and c_K^L being dimensionless. If only the lowest, $L = 2$, terms are kept, one obtains the real potential[25,26]

$$u(\Omega_{CM}) = -c_0^2 D_{0,0}^2(\Omega_{CM}) - c_2^2\left[D_{0,2}^2(\Omega_{CM}) + D_{0,-2}^2(\Omega_{CM})\right] \quad (4)$$

Note that we did not consider the lowest $L = 1$ terms. They could be considered[33] but are typically omitted in view of the second-rank ($L = 2$) nature of the quadrupolar tensor.[34]

The order parameters for $L = 2$ are defined as[25]

$$\left\langle D_{0,K}^2(\Omega_{CM})\right\rangle = \int d\Omega_{CM} D_{0,K}^2(\Omega_{CM}) \exp[-u(\Omega_{CM})] \Big/ \int d\Omega_{CM} \exp[-u(\Omega_{CM})],\ K = 0, 2 \quad (5)$$

For at least three-fold symmetry around the local director, C, and at least two-fold symmetry around the principal axis of the local ordering tensor, $\mathbf{Z}_M$, only the irreducible tensor components $S_0^2 \equiv \left\langle D_{0,0}^2(\Omega_{CM})\right\rangle$ and $S_2^2 \equiv \left\langle D_{0,2}^2(\Omega_{CM}) + D_{0,-2}^2(\Omega_{CM})\right\rangle$ survive.[25] The Cartesian order parameters relate to S_0^2 and S_2^2 as

$$S_{xx} = \left(\sqrt{3/2}S_2^2 - S_0^2\right)/2$$
$$S_{yy} = -\left(\sqrt{3/2}S_2^2 + S_0^2\right)/2$$
$$S_{zz} = S_0^2$$

In this study, the potential of eq 4 is enhanced to also include the $L = 4$, $K = 0$ and $L = 4$, $K = 2$ terms; its form is given by

$$u(\Omega_{CM}) = -c_0^2 D_{00}^2(\Omega_{CM}) - c_2^2\left[D_{0,2}^2(\Omega_{CM}) + D_{0,-2}^2(\Omega_{CM})\right] - c_0^4 D_{00}^4(\Omega_{CM}) - c_2^4\left[D_{0,2}^4(\Omega_{CM}) + D_{0,-2}^4(\Omega_{CM})\right] \quad (6)$$

The implementation of the MOMD approach is described in refs 27 and 35. Reference 35 is a User's Guide for the calculation of slow-motional Magnetic Resonance spectra (here, ^{2}H spectra) for given values of Ω_{LC}. Reference 27 is the article where MOMD was originally described; the superposition of individual slow-motional (EPR) lineshapes according to a random distribution of Ω_{LC} is discussed in some detail in that article.

To carry out a MOMD calculation, one has to specify the external magnetic field, the quadrupole coupling constant, Q, the intrinsic line width, $(1/T_2^*)$, the number of Ω_{LC} values for which slow-motional lineshapes are to be calculated, and the technical parameters associated with the calculation of slow-motional (NMR or ESR) spectra.[35] The physical parameters to be specified and varied in the data-analysis, include the coefficients of the

potential (c_0^2 and c_2^2 for the potential of eq 4, and c_0^2, c_2^2, c_0^4, and c_2^4 for the potential of eq 6), the diffusion rate constants $R_\parallel$ and $R_\perp$, and the "diffusion tilt", β_{MQ}.

3. RESULTS AND DISCUSSION

3.1. Qualitative Analysis of the N-Terminal ^{2}H Spectra.

Experimental ^{2}H lineshapes from residues A2, F4, τ-H6, and G9 of the N-terminal domain of the three-fold-symmetric twisted polymorph of the Aβ_{40}-amyloid fibril,[6] also used in ref 21, are employed. The generic probes are CD_3 and C–D. In a broader stereochemical context the rigid structural moieties that serve as probes are C^α–$C^\beta D_3$ for A2, C^β-phenyl-d_5 for F4, the (N-ring)-CD_3 for τ-H6, and C^α–D for G9 (because of limited temperature-dependence, the ^{2}H spectrum of C^β–$(C^\gamma D_3)_2$ of V12 was only shown for illustration in ref 21 but not further analyzed; we disregard it here). The information delineated in this paragraph is summarized in Table 1. Figure 2 shows (a) a schematic of the monomer (PDB ID 2LMP, which includes residues 9 and beyond)[6] and (b) an extended schematic of the monomer which also includes the N-terminal section 1–9 as a straight line. The residues studied here with the respective probes given in Table 1 are depicted in Figure 2b.

The rigid-limit quadrupole constants, Q, of quadrupole tensors considered to be axially symmetric, were taken from ref 21. For the aliphatic deuterons, Q ranges from 155 kHz for G9 to 165.5 kHz for A2; for phenyl-d_5 one has $Q = 180$ kHz. Should very fast local fluctuations be in effect, these values will be reduced somewhat. Should very fast methyl rotation be in effect, Q is reduced to $\langle Q \rangle = [1.5 \cos^2(109.5°) - 0.5] \times Q = 0.332 \times Q$. We focus below on the shapes of the ^{2}H spectra and their variation as a function of temperature.

Figure 3 shows side-by-side the temperature-dependent experimental ^{2}H spectra of A2 and G9 which are typical sets, as shown below. Generally, all of them exhibit a peaklike feature at $\omega = 0$ kHz and two flanking divergences located at $\pm 3/8 Q$ kHz for G9 and $\pm 3/8 \langle Q \rangle$ for A2. The latter are the perpendicular divergences of the corresponding rigid limit spectra. The evolution of the two sets of spectra with temperature does not differ much; spectra resembling one another in shape appear at temperatures that are approximately 15 K lower for glycine. In addition, for G9 the $\omega = 0$ peaklike feature is narrower than the flanking divergences whereas for A2 all three features are comparable in width. A typical example is provided by the 271 K spectrum of G9 and the 257 K spectrum of A2. Evidently, important characteristics of the respective dynamic structures differ.

Let us compare the ^{2}H spectra of C^α–$C^\beta D_3$ of A2 and the (N-ring)–CD_3 of τ-H6 (Figure S2). The evolution as a function of temperature of these two sets is generally similar and spectra resembling one another in shape appear at comparable temperatures. Both residues considered comprise the generic probe, CD_3, in different structural settings. Figure S3 shows side-by-side the spectra of F4 and G9. Both residues comprise the generic probe, C–D, in a sidechain aromatic setting for F4 and a mainchain aliphatic setting for G9. As in Figure 3, the evolution with temperature of the two sets of spectra does not differ much and spectra similar in shape appear at temperatures that are lower by approximately 15 K for G9. Likewise, the $\omega = 0$ peaklike is narrower than the flanking divergences for G9. Finally, the A2 and F4 spectra are shown side-by-side in Figure S4. They evolve similarly and exhibit

similar shapes at comparable temperatures, despite substantial diversity in CD_3 attachment to the residue framework.

Quite clearly, Figures 3 and S2–S4 distinguish G9 as residue yielding ^{2}H spectra differing in character from the ^{2}H spectra of all the other residues studied. Consequently, for quantitative analysis we group the four residues investigated into two categories: G9 on the one hand and A2, τ-H6, and F4 on the other hand.

3.2. Relevant Parameter Ranges.

The local diffusion tensor, $\boldsymbol{R}$, is taken to be axially symmetric with principal values $R_\parallel$ and $R_\perp$ (in s^{-1}); in discussing simulations, we report them as log $R_\parallel$ and log $R_\perp$. On the logarithmic scale, the dynamic window extends from about 2.2 to about 6.2.

As indicated, the local potential, u, is expanded in the basis set of the real even-L Wigner functions, $D^L_{0|K|} = \left[D^L_{0-K} + (-1)^K D^L_{0K}\right]$. This expansion has to be truncated prior to applying MOMD to actual experimental spectra. The simplest axial potential is $u = -c^2_0 D^2_{00}$ and the simplest rhombic potential is $u = -c^2_0 D^2_{00} - c^2_2 D^2_{0|K|}$. Adding the next two terms of the expansion yields the potential $u = -c^2_0 D^2_{00} - c^2_2 D^2_{0|2|} - c^4_0 D^4_{00} - c^4_2 D^4_{0|2|}$. Thus far, we found that the local potential at the site of the motion of methyl and phenyl moieties in proteins is weak.[16,19,20,22,23]

3.3. Quantitative Analysis of the Experimental ^{2}H Spectra.

3.3.1. General Considerations.—Upon raising the temperature, globally the relative intensity of the $\omega = 0$ peaklike feature increases at the expense of the perpendicular divergences. ^{2}H spectra from a selectively ^{2}H-labeled polyethylene chain exhibiting similar features were reproduced with two-fold C–D jumps around the tetrahedral angle bisector.[31] In MOMD nomenclature, this corresponds to $\beta_{MQ} = 54.8°$. However, the shapes of those spectra differ considerably from the ^{2}H lineshapes considered here, so this simple model is not appropriate in the present case,

In a later study, the authors of ref 31 published ^{2}H lineshapes closer in appearance to those of the N-terminal domain.[11] This was accomplished by including into the model a double-well potential 5 kT in height and replacing the discrete jumps by simple diffusion. We found that the model suggested in ref 31 is still not suitable in the present case: one has to generalize the potential, and/or lower the symmetry of the diffusive motion, and/or raise the restriction of motion occurring exclusively around the tetrahedral angle bisector. MOMD allows for these features.

With regard to the phenyl-d_5 probe of F4, the simplest model for a description of the dynamics are 180°-jumps around its symmetry axis. This corresponds to $\beta_{MQ} = 60°$. Schadt et al.[36] have shown that considering diffusive motion instead of discrete jumps leads to $\beta_{MQ} = 64°$. $\beta_{MQ} = 54.8°$ for aliphatic C–D bonds and $\beta_{MQ} = 64°$ for the C–D bonds of F4 may be considered as reference points in comparing actual diffusion tilts.

3.3.2. Quantitative MOMD Analysis.—Figure 4 shows simulated MOMD spectra obtained with the potential of eq 4 and an axial local diffusion tensor. Specifically, we used $c_0^2 = 2.2$, log $R_\perp = 2.2$, $\langle Q \rangle = 52.8$ kHz, and c_2^2 and log $R_\parallel$ as depicted in the figure. $R_\perp$ is given in units of 10^2 s^{-1} and $R_\parallel$ in units of 10^4 s^{-1}. The diffusion tilt, β_{MQ}, is varied from 90 to 130°, illustrating the great effect this polar angle has on the analysis. On the basis of comparison with the experimental ^{2}H spectra, we found that $R_\perp$ is mostly close to its rigid-limit, that is, log $R_\perp = 2.2$, c_0^2 and c_2^2 are on the order of 2–3, and β_{MQ} is in the 50°–60° range. Using these parameter ranges and allowing $R_\parallel$ to vary over the entire dynamic range, we still could not satisfactorily reproduce the main features of the individual ^{2}H lineshapes and their evolution as a function of temperature.

A component of the MOMD model to which the analysis is particularly sensitive is the shape of the local potential.[16,19,20,22,23,32] This is illustrated in Figure 5. As indicated in Theoretical Background, the MOMD spectrum is obtained by summing spectra with $0° \leq \beta_{LC} \leq 90°$, where β_{LC} denotes the orientation of a given crystallite with respect to the dc magnetic field of the NMR spectrometer (Figure 1). We calculated component ^{2}H spectra for nine β_{LC} values, with $R_\perp$, $R_\parallel$, the coefficients of the local potential in the relevant parameter ranges, and $\beta_{MQ} = 54°$. Figure 5a shows the ^{2}H lineshapes obtained for the potential of eq 4 with $c_0^2 = c_2^2 = 2$. Figure 5b shows the ^{2}H lineshapes obtained for the potential of eq 6 with $c_0^2 = c_2^2 = 2$, $c_0^4 = 0.5$, and $c_2^4 = -2$ found to be typical (see below). It can be seen that the four-term potential yields lineshapes that are considerably more complex and better resolved than the two-term potential, hence expected to be more effective in fitting the experimental lineshapes. We proceed using the potential of eq 6.

Figure 6a shows the experimental ^{2}H spectra of the C^α–$C^\beta D_3$ probe of A2. Following extensive simulations, we obtained the best-fit spectra shown in Figure 6b; the corresponding best-fit parameters are given in Table 2.

From 247 to 271 K, experimental spectra were recorded at small intervals (10, 10, and 4 K); the next spectrum was recorded at 310 K (39 K interval). In the 247–271 K range, $R_\perp$ is near its rigid limit (1.6×10^2 s^{-1}), and $R_\parallel$ increases gradually from 2.0×10^4 to 2.0×10^5 s^{-1}. The activation energy associated with $R_\parallel$ is 53 ± 1.9 kJ/mol (Figure 7a; cf. Figure 7b for comparison). At 310 K, satisfactory fit was obtained for $R_\perp = 5.0 \times 10^3$ s^{-1}, $R_\parallel = 5.0 \times 10^5$ s^{-1}, and an axial potential comprising both D_{00}^2 and D_{00}^4. Data paucity and spectrum simplicity at high temperature does not enable determining c_2^2 and c_2^4. The 310 K description should be considered to be the axial approximation to the genuine rhombic-potential-based description. All of the spectra have been reproduced with $\beta_{MQ} = 58°$.

Figure 8a shows the experimental ^{2}H spectra of the C^α–D probe of G9; Figure 8b shows the MOMD spectra that generated the best agreement with the corresponding parameters given in Table 3. $R_\perp$ is near its rigid limit in the 271–280 K range; in the 280–310 K range it increases up to 4.0×10^2 s^{-1}. $R_\parallel$ increases from 3.2×10^5 s^{-1} at 271 K to 1.0×10^6 s^{-1} at 310 K. The activation energy associated with $R_\parallel$ is 19.3 ± 2.2 kJ/mol (Figure 7b). All of the spectra are reproduced with $\beta_{MQ} = 54°$.

We wish to comment on the narrow peaklike feature at $\omega = 0$ in the experimental 271 and 280 K spectra of G9 (Figure 8a) not being reproduced well by MOMD. The MOMD analysis is very sensitive to β_{MQ}[16,19,20,22,23] (see also Figure 4). Varying the other polar angle between the M and Q frames, α_{MQ}, currently fixed at zero, is likely to improve the fit. By also allowing for $R_{xx} \neq R_{yy}$ (currently set equal to one another), it is very likely that the overall agreement between the MOMD spectra and the experimental spectra will be improved. This is postponed to future work, when the noted enhancements will have been implemented in the MOMD software package.

Let us compare the results obtained for A2 and G9. The G9 potentials are stronger (larger c_0^2 and c_0^4, on average) and more rhombic (larger c_2^2 and $|c_0^4|$, on average) than the A2 potentials. At the same temperatures, $R_\parallel$ is considerably larger for G9 than for A2. Figures 3 and S2–S4 show that the ^{2}H spectra of F4 and τ-H6 are similar both in shape at specific temperatures, and in their evolution as a function of temperature to the ^{2}H spectra of A2. As indicated, residue G2 is an outlier. Table 1 shows that C^α–D of G9 is the only probe which comprises a main-chain atom. We suggest that this feature is the dominant factor in causing a more restrictive and substantially rhombic environment which stimulates faster nonsymmetric local probe motion.

3.3.3. Comparison between the N-Terminal and Core Domains.—Figure 9 compares the ^{2}H spectra of A2 from the N-terminal domain (right column) with the ^{2}H spectra of M35 from the core domain (left column, red).[19] The 257 K spectrum of A2 and the 238 K spectrum of M35 illustrate the emergence of the $\omega = 0$ peaklike feature (flanked by the perpendicular $\omega = \pm 3/8\langle Q \rangle$ kHz divergences). The central part of the A2 spectrum is much better resolved. The two sets of spectra evolve differently with increasing temperature. For example, the region between the $\omega = 0$ peaklike feature and the perpendicular divergences is convex in the 258 K M35 spectrum and concave in the 262 K A2 spectrum.

The M35 spectrum changes discontinuously between 258 and 274 K. This is caused by the 260 K freezing of bulklike water in the fibril matrix transmitted to the fibril structure by interaction with tightly peptide-bound water.[19] From the MOMD perspective the shape of the local potential, and the local geometry, change suddenly around 260 K. As determined in ref 19, one has $c_0^2 = 19$, $c_2^2 = 2.3$, and $\beta_{MQ} = 65°$ at 258 K, and $c_0^2 = 2.4$, $c_2^2 = 1.9$, and $\beta_{MQ} = 60°$ at 274 K; this represents a substantial change in the shape of the local potential, and the magnitude of the diffusion tilt.

On the other hand, the A2 spectrum changes gradually; note the weak perpendicular divergences in the 271 K spectrum. This is consistent with the absence of tightly peptide-bound water in the N-terminal domain without which the 260 K freezing event cannot be transmitted to the fibril structure. We recall that MSM suggests that a phase transition does take place in the N-terminal at 260 K.

It is of interest to compare best-fit parameters of an N-terminal domain CD_3 spectrum and a core domain CD3 spectrum at the same temperature. The 257 K MOMD spectrum of A2

(Figure 6b) and the 258 K MOMD spectrum of M35 (ref 19) are suitable in this context; the respective data are given in Table 4.

Inspection of Table 4 shows that the local potential is more complex in the N-terminal domain than in the core domain. Although the M35 potential is simpler, the main diffusion/ordering axis of this core residue is much farther from the 54.8° reference point than the main diffusion/ordering axis of A2. The activation energies for $R_{\|}$ are (19.3 ± 2.2) kJ/mol for A2 (Figure 7b) and 5.9 ± 0.2 kJ/mol for M35 (ref 13). As indicated, M35 resides at the fibril interface where it interacts with tightly peptide-bound water;[19] This might cause at least partly the low activation energy obtained.

The structural dynamics of the Aβ-amyloid N-terminal domain determined here refers to the three-fold-symmetric twisted Aβ_{1-40} polymorph. N-terminal domains of other Aβ-amyloid polymorphs may exhibit different structural dynamics.[37–40]

4. CONCLUSIONS

The MOMD model for the analysis of NMR lineshapes in the solid-state was applied to the N-terminal domain of Aβ_{40}-amyloid fibrils ^{2}H-labeled at residues A2, F4, τ-H6, and G9. It was found that the spatial restrictions at the site of the motion of the pertinent probes are adequately represented by four-term rhombic potentials that are 2–3 kT in magnitude. The local motion is adequately described by an axial diffusion tensor, $\boldsymbol{R}$, with slow perpendicular component and intermediate-to-fast parallel component. For the aliphatic C–D and C–CD_3 bonds, the orientation of $\boldsymbol{R}$ digresses by just a few degrees from the tetrahedral angle bisector.

The C^{α}–D bonds of G9 are outliers. These are the only probes comprising a mainchain atom. Its presence produces stronger local restrictions and faster (nonsymmetric) local probe motion.

In previous work, MOMD was applied to the core domain of the Aβ_{40}-amyloid fibril. That interpretation of structural dynamics and the current interpretation of N-terminal domain structural dynamics are similar in essence. They differ in parameter magnitude and complexity.

This study has shown that MOMD is a useful tool for studying molecular environments in protein aggregates.

Supplementary Material

Refer to Web version on PubMed Central for supplementary material.

ACKNOWLEDGMENTS

This work was supported by the Israel-U.S.A. Binational Science Foundation (Grant 2016097 to E.M. and J.H.F.), and the Israel Science Foundation (Grant 288/20 to E.M.). This work was also supported by NIH/NIGMS Grant P41GM103521 to J.H.F.

REFERENCES

(1). Harrison PS; Sharpe PC; Singh Y; Fairlie DP Amyloid Peptides and Proteins in Review. Rev. Physiol. Biochem. Pharmacol 2007, 159, 1–77. [PubMed: 17846922]

(2). Paravastu AK; Qahwash I; Leapman RD; Meredith SC; Tycko R Seeded Growth of β–Amyloid Fibrils from Alzheimer's Brain-Derived Fibrils Produces a Distinct Fibril Structure. Proc. Natl. Acad. Sci. U. S. A 2009, 106, 7443–7448. [PubMed: 19376973]

(3). van der Wel PCA Insights into Protein Misfolding and Aggregation Enabled by Solid-State NMR Spectroscopy. Solid State Nucl. Magn. Reson 2017, 88, 1–14. [PubMed: 29035839]

(4). Wälti MA; Ravotti F; Arai H; Glabe CG; Wall JS; Böckmann A; Güntert P; Meier BH; Riek R Atomic-Resolution Structure of a Disease-Relevant Aβ(1–42) Amyloid Fibril. Proc. Natl. Acad. Sci. U. S. A 2016, 113, E4976–E4984. [PubMed: 27469165]

(5). Petkova AT; Yau W-M; Tycko R Experimental Constraints on Quaternary Structure in Alzheimer's β-Amyloid Fibrils. Biochemistry 2006, 45, 498–512. [PubMed: 16401079]

(6). Paravastu AK; Leapman RD; Yau W-M; Tycko R Molecular Structural Basis for Polymorphism in Alzheimer's β-Amyloid Fibrils. Proc. Natl. Acad. Sci. U. S. A 2008, 105, 18349–18354. [PubMed: 19015532]

(7). Fitzpatrick AWP; Debelouchina GT; Bayro MJ; Clare DK; Caporini MA; Bajaj VS; Jaroniec CP; Wang L; Ladizhansky V; Muller SA; MacPhee CE; Waudby CA; Mott HR; De Simone A; Knowles TPJ; Saibil HR; Vendruscolo M; Orlova EV; Griffin RG; Dobson CM Atomic Structure and Hierarchial Assembly of a cross-β Amyloid Fibril. Proc. Natl. Acad. Sci. U. S. A 2013, 110, 5468–5473. [PubMed: 23513222]

(8). Cerofolini L; Ravera E; Bologna S; Wiglenda T; Boddrich A; Purfurst B; Benilova I; Korsak M; Gallo G; Rizzo D; Gonnelli L; Fragai M; De Strooper B; Wanker EE; Luchinat C et al. Mixing Aβ(1–40) and Aβ(1–42) Peptides Generates Unique Amyloid Fibrils. Chem. Commun 2020, 56, 8830–8833.

(9). Tornquist M; Cukalevski R; Weininger U; Meisl G; Knowles TPJ; Leiding T; Malmendal A; Akke M; Linse S Ultrastructural Evidence for Self-Replication of Alzheimer-Associated Aβ42 Amyloid Along the Sides of Fibrils. Proc. Natl. Acad. Sci. U.S.A 2020, 117, 11265–11273. [PubMed: 32439711]

(10). Almeida ZL; Brito RMM Structure and Aggregation Mechanisms in Amyloids. Molecules 2020, 25, 1195–1125.

(11). Wittebort RJ; Olejniczak ET; Griffin RG Analysis of Deuterium Nuclear Magnetic Resonance Line Shapes in Anisotropic Media. J. Chem. Phys 1987, 86, 5411–5420.

(12). Vold RL; Hoatson GL Effects of Jump Dynamics on Solid State Nuclear Magnetic Resonance Line Shapes and Spin Relaxation Times. J. Magn. Reson 2009, 198, 57–72. [PubMed: 19201232]

(13). Guan H; Li J; Zhou T; Pang Z; Fu Y; Cornelio J; Wang Q; Telfer SG; Kong X Probing Non-Uniform Adsorption in Multicomponent Metal-Organic Frameworks via Segmental Dynamics by Solid State Nuclear Magnetic Resonance. J. Phys. Chem. Lett 2020, 11, 7167–7176. [PubMed: 32787305]

(14). Reif B; Ashbrook SE; Emsley L; Hong M Solid-State NMR Spectroscopy. Nature Reviews (Methods Primers) 2021, 1, 2.

(15). Vugmeyster L Recent Developments in Deuterium Solid-State NMR for the Detection of Slow Motions in Proteins. Solid State NMR 2021, 111, 101710.

(16). Meirovitch E; Liang Z; Freed JH Protein Dynamics in the Solid State from ^{2}H NMR Line Shape Analysis: A Consistent Perspective. J. Phys. Chem. B 2015, 119, 2857–2868. [PubMed: 25594631]

(17). Vugmeyster L; Clark MA; Falconer IB; Ostrovsky D; Gantz D; Qiang W; Hoatson GL Flexibility and Solvation of Amyloid-β Hydrophobic Cores. J. Biol. Chem 2016, 291, 18484–18495. [PubMed: 27402826]

(18). Vugmeyster L; Ostrovsky D; Hoatson GL; Qiang W; Falconer IB Solvent-Driven Dynamical Crossover in the Phenylalanine Side-Chain from the Hydrophobic Core of Amyloid Fibrils Detected by ^{2}H NMR Relaxation. J. Phys. Chem. B 2017, 121, 7267–7275. [PubMed: 28699757]

(19). Meirovitch E; Liang Z; Freed JH MOMD Analysis of NMR Lineshapes from Aβ-Amyloid Fibrils: A New Tool for Characterizing Molecular Environments in Protein Aggregates. J. Phys. Chem. B 2018, 122, 4793–4801. [PubMed: 29624402]

(20). Meirovitch E; Liang Z; Freed JH Phenyl-Ring Dynamics in Amyloid Fibrils and Proteins: The Microscopic-Order-Macroscopic-Disorder Perspective. J. Phys. Chem. B 2018, 122, 8675–8684. [PubMed: 30141954]

(21). Au DF; Ostrovsky D; Fu R; Vugmeyster L Solid-State NMR Reveals a Comprehensive View of the Dynamics of the Flexible Disordered N-Terminal Domain of Amyloid-β Fibrils. J. Biol. Chem 2019, 294, 5840–5853. [PubMed: 30737281]

(22). Meirovitch E; Liang Z; Freed JH Protein Dynamics in the Solid State from ^{2}H NMR Line Shape Analysis. II. MOMD Applied to C–D and C–CD_3 probes. J. Phys. Chem. B 2015, 119, 14022–14032. [PubMed: 26402431]

(23). Meirovitch E; Liang Z; Freed JH Structural Dynamics by NMR in the Solid State: The Unified MOMD Perspective Applied to Organic Frameworks with Interlocked Molecules. J. Phys. Chem. B 2020, 124, 6225–6235. [PubMed: 32584038]

(24). Polnaszek CF; Bruno GV; Freed JH ESR Lineshapes in the Slow-Motional Region: Anisotropic Liquids. J. Chem. Phys 1973, 58, 3185–3199.

(25). Polnaszek CF; Freed JH Electron Spin Resonance Studies of Anisotropic Ordering, Spin Relaxation, and Slow Tumbling in Liquid Crystalline Solvents. J. Phys. Chem 1975, 79, 2283–2306.

(26). Lin WJ; Freed JH Electron Spin Resonance Studies of Anisotropic Ordering, Spin Relaxation, and Slow Tumbling in Liquid Crystalline Solvents: 3. Smectics. J. Phys. Chem 1979, 83, 379–401.

(27). Meirovitch E; Nayeem A; Freed JH Protein-Lipid Interactions: A Single-Site Interpretation of the ESR Spectra. J. Phys. Chem 1984, 88, 3454–3465.

(28). NMR of Liquid Crystals; Emsley JW, Ed.; Reidel Dordrecht, 1983.

(29). The Molecular Dynamics of Liquid Crystals; Luckhurst GR; Veracini CA, Eds.; Kluwer Academic Publishers: The Netherlands, 1994.

(30). Vugmeyster L; Au DF; Ostrovsky D; Fu R Deuteron Solid-State NMR Relaxation Measurements Reveal Two Distinct Conformational Exchange Processes in the Disordered N-Terminal Domain of Amyloid-β Fibrils. ChemPhysChem 2019, 20, 1680–1689. [PubMed: 31087613]

(31). Huang TH; Skarjune RP; Wittebort RJ; Griffin RG; Oldfield E Restricted Rotational Isomerization in Polyethylene Chains. J. Am. Chem. Soc 1980, 102, 7377–7381.

(32). Meirovitch E; Liang Z; Freed JH Protein Dynamics in the Solid State from ^{2}H NMR Line Shape Analysis. III. MOMD in the Presence of Magic Angle Spinning. Solid State Nucl. Magn. Reson 2018, 89, 35–44. [PubMed: 29208317]

(33). Tchaicheeyan O; Freed JH; Meirovitch E Local Ordering at Mobile Sites in Proteins from Nuclear Magnetic Resonance Relaxation: The Role of Site Symmetry. J. Phys. Chem. B 2016, 120, 2886–2898. [PubMed: 26938937]

(34). Polimeno A; Freed JH A Many-Body Stochastic Approach to Rotational Motions in Liquids. Adv. Chem. Phys 2007, 83, 89–204.

(35). Schneider DJ; Freed JH Calculating Slow Motional Magnetic Resonance Spectra: A User Guide. In Biological Magnetic Resonance; Plenum: New York, 1989; Vol. 8, pp 1–76.

(36). Schadt RJ; Cain EJ; English AD Simulation of One-Dimensional ^{2}H NMR Line Shapes. J. Phys. Chem 1993, 97, 8387–8392.

(37). Yang M; Teplow DB Amyloid β-Protein Monomer Folding. J. Mol. Biol 2008, 384, 450–464. [PubMed: 18835397]

(38). Xu L; Chen Y; Wang X Dual Effects of Familial Alzheimer's Disease Mutations (D7H, D7N and H6R) on Amyloid β Peptide: Correlation Dynamics and Zinc binding. Proteins 2014, 82, 3286–3297. [PubMed: 25137638]

(39). Sgourakis NG; Yan Y; McCallum SA; Wang C; Garcia AE The Alzheimer's Peptides Aβ40 and 42 Adopt Distinct Conformations in Water: A Combined MD/NMR Study. J. Mol. Biol 2007, 368, 1448–1457. [PubMed: 17397862]

(40). Ono K; Condron MM; Teplow DB Effect of the English (H6R) and Tottori (D7N) Familial Alzheimer Disease Mutations on Amyloid β-Protein Assembly and Toxicity. J. Biol. Chem 2010, 285, 23186–23197. [PubMed: 20452980]

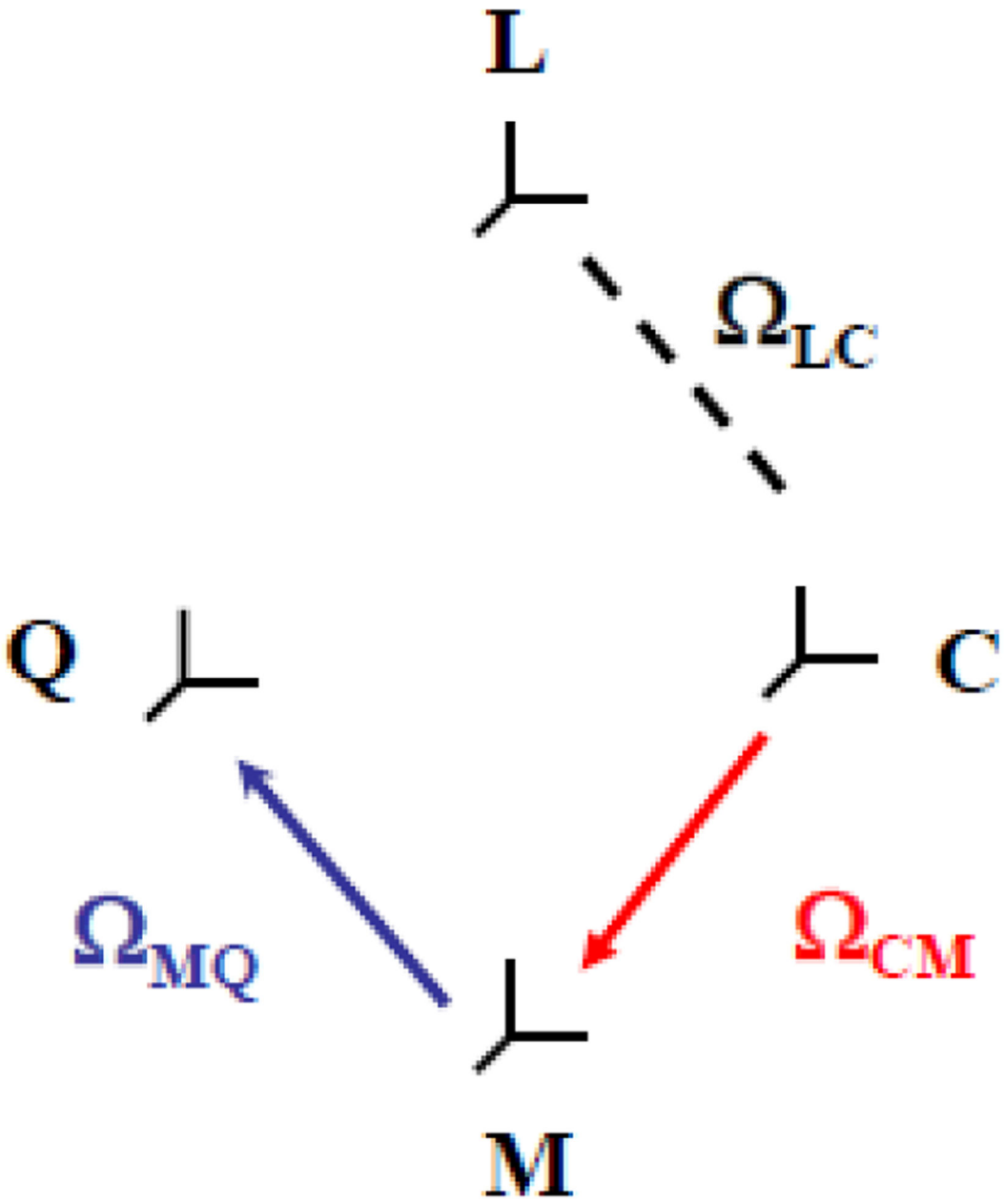

Figure 1.
^{2}H/MOMD frame structure. L, space-fixed laboratory frame; C, molecule-fixed axial local director frame with principal axis pointing along the average orientation of the probe; M, probe-fixed ordering/diffusion frame; Q, probe-fixed quadrupolar frame.[10]

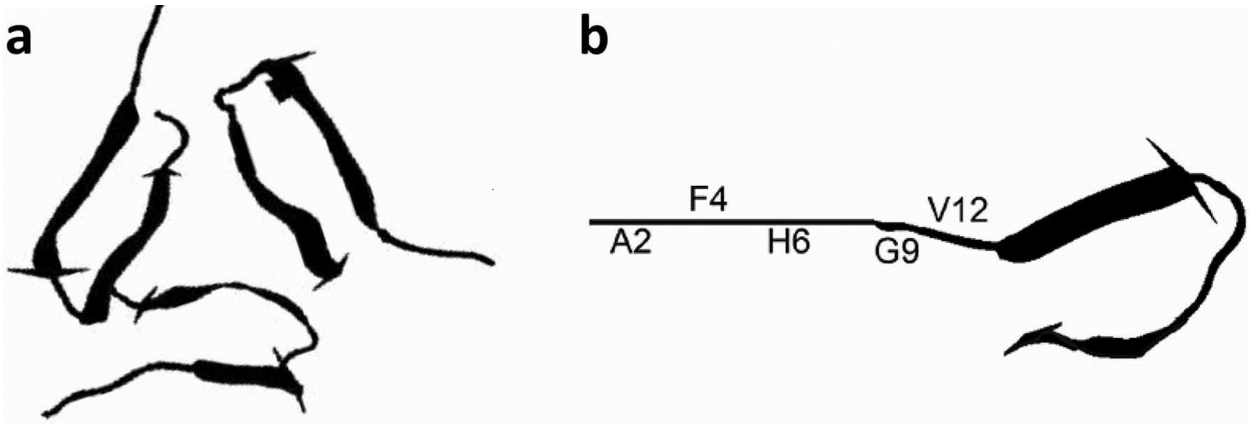

Figure 2.

(a) A schematic of the monomer, taken from PDB ID 2LMP; the X-ray crystallography structure includes the residues beyond residue 9 (ref 6). (b) Extension of the schematic of part b to also include residues 1–9, represented by a straight line. The residues considered in this study are depicted in Figure 2b. Reproduced with permission from Au, D. F.; Ostrovsky, D.; Fu, R.; Vugmeyster, L. Solid-State NMR Reveals a Comprehensive View of the Dynamics of the Flexible Disordered N-Terminal Domain of Amyloid-β Fibrils. *J. Biol. Chem.* **2019**, *294*, 5840–5853. Copyright 2019 of the American Society for Biochemistry and Molecular Biology.

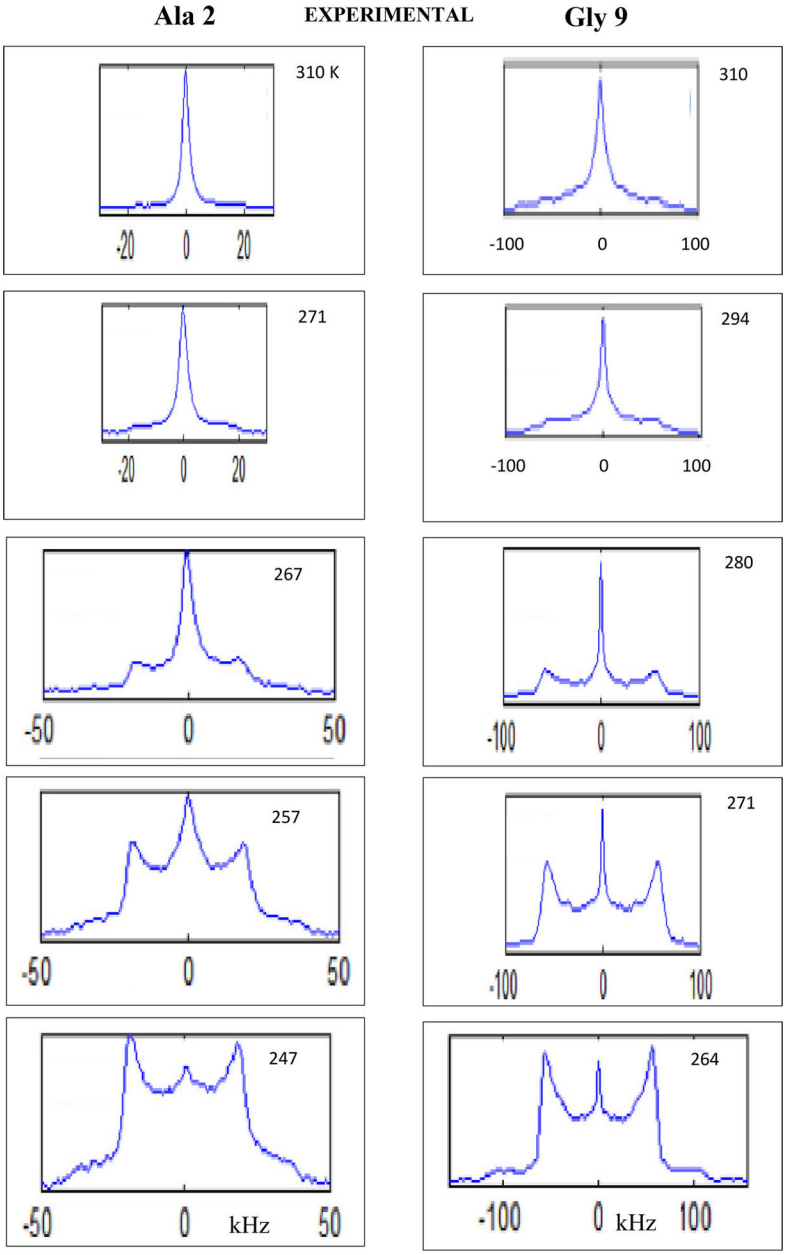

Figure 3.

Experimental ^{2}H lineshapes from the C^{α}–$C^{\beta}D_3$ probe of residue A2 (left) and the C^{α}–D probe of residue G9 (right), at the temperatures given in the figure. Reproduced with permission from Au, D. F.; Ostrovsky, D.; Fu, R.; Vugmeyster, L. Solid-State NMR Reveals a Comprehensive View of the Dynamics of the Flexible Disordered N-Terminal Domain of Amyloid-β Fibrils. *J. Biol. Chem.* **2019**, *294*, 5840–5853. Copyright 2019 of the American Society for Biochemistry and Molecular Biology.

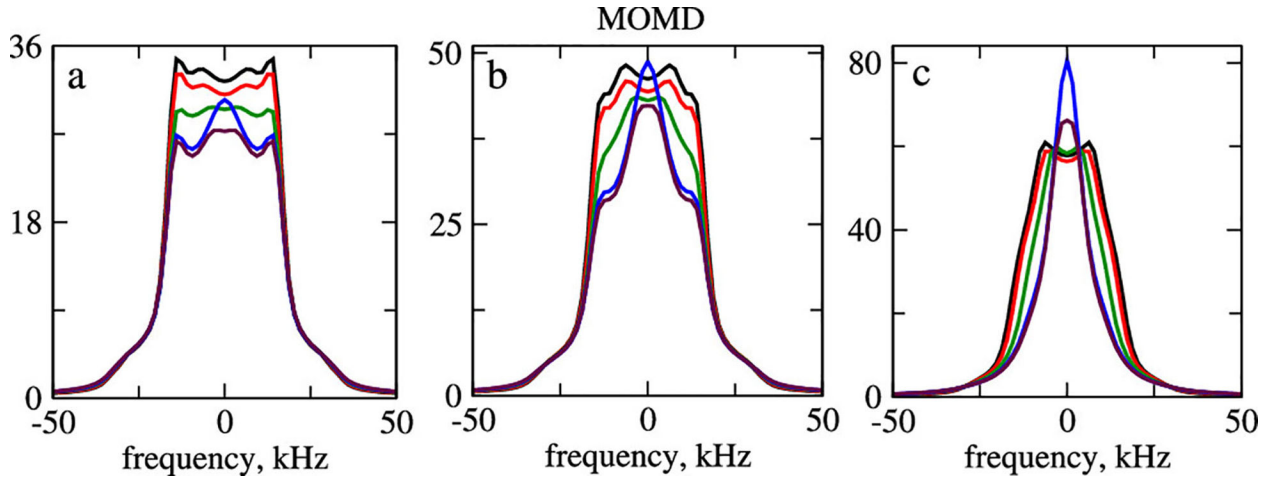

Figure 4.

^{2}H MOMD spectra obtained for $c_0^2 = 2.2$, $R_\perp = 1.6 \times 10^2$ s^{-1} and (a) $c_2^2 = 1.8$ and log $R_\parallel = 2.0$ ($R_\parallel = 1.0 \times 10^2$ s^{-1}); (b) $c_0^2 = 2.6$ and log $R_\parallel = 3.16$ ($R_\parallel = 1.5 \times 10^4$ s^{-1}); (c) $c_0^2 = 2.8$ and log $R_\parallel = 5.01$ ($R_\parallel = 1.0 \times 10^5$ s^{-1}). The colors designating β_{MQ} are as follows: 90° (black), 100° (red), 110° (green), 120° (blue), and 130° (violet). Additional parameters used include $\langle Q \rangle$ = 52.8 kHz and intrinsic line width of 1 kHz.

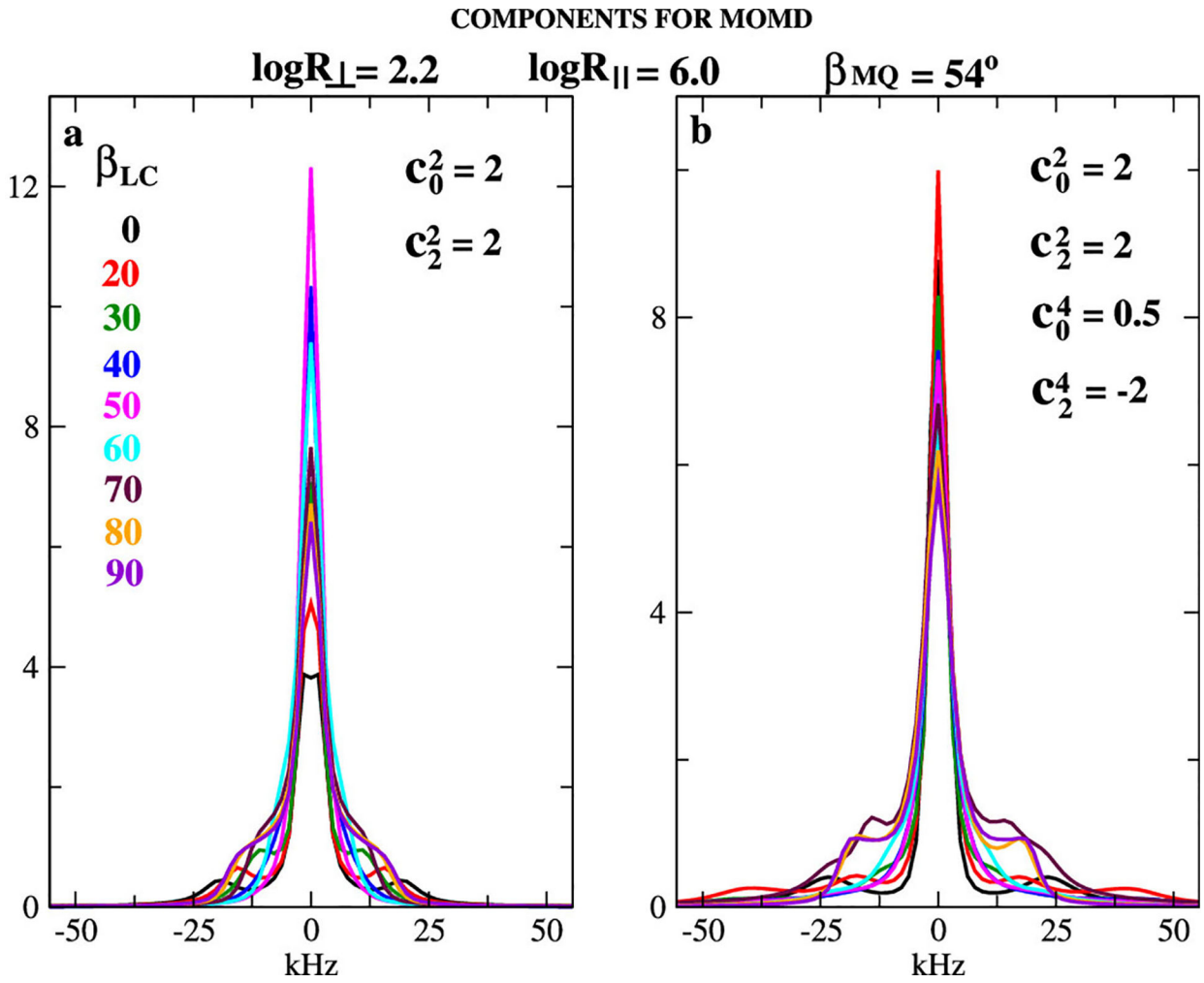

Figure 5.

Components of MOMD spectra specified by nine β_{LC} values in the 0–90° range, colored as shown. These individual spectra yield by summation the MOMD spectra with $R_{\perp} = 2.2$, log $R_{\parallel} = 6.0$, $\beta_{MQ} = 54°$ and (a) the axial potential of eq 4 with $c_0^2 = 2$ and $c_2^2 = 2$, (b) the rhombic potential of eq 6 with $c_0^2 = 2$, $c_2^2 = 2$, $c_0^4 = 0.5$, and $c_2^4 = -2$.

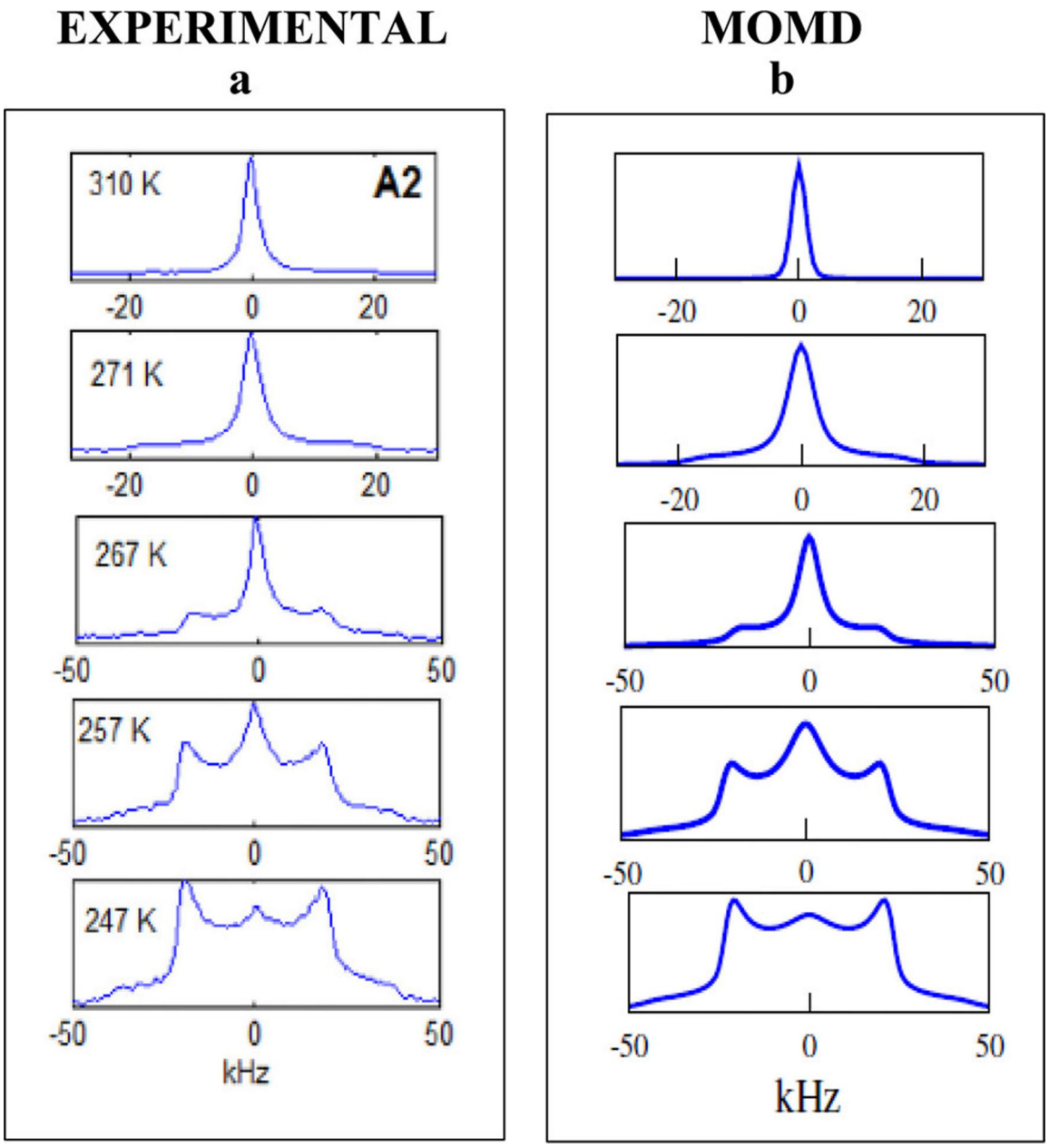

Figure 6.

(a) Experimental ^{2}H spectra of the C^{α}–$C^{\beta}D_3$ probe of residue A2 at the temperatures given in the figure. Reproduced with permission from Au, D. F.; Ostrovsky, D.; Fu, R.; Vugmeyster, L. Solid-State NMR Reveals a Comprehensive View of the Dynamics of the Flexible Disordered N-Terminal Domain of Amyloid-β Fibrils. *J. Biol. Chem.* **2019**, *294*, 5840–5853. Copyright 2019 of the American Society for Biochemistry and Molecular Biology. (b) ^{2}H MOMD spectra that fit best the experimental spectra in (a). The best-fit MOMD parameters used in the (b) spectra are given in Table 2.

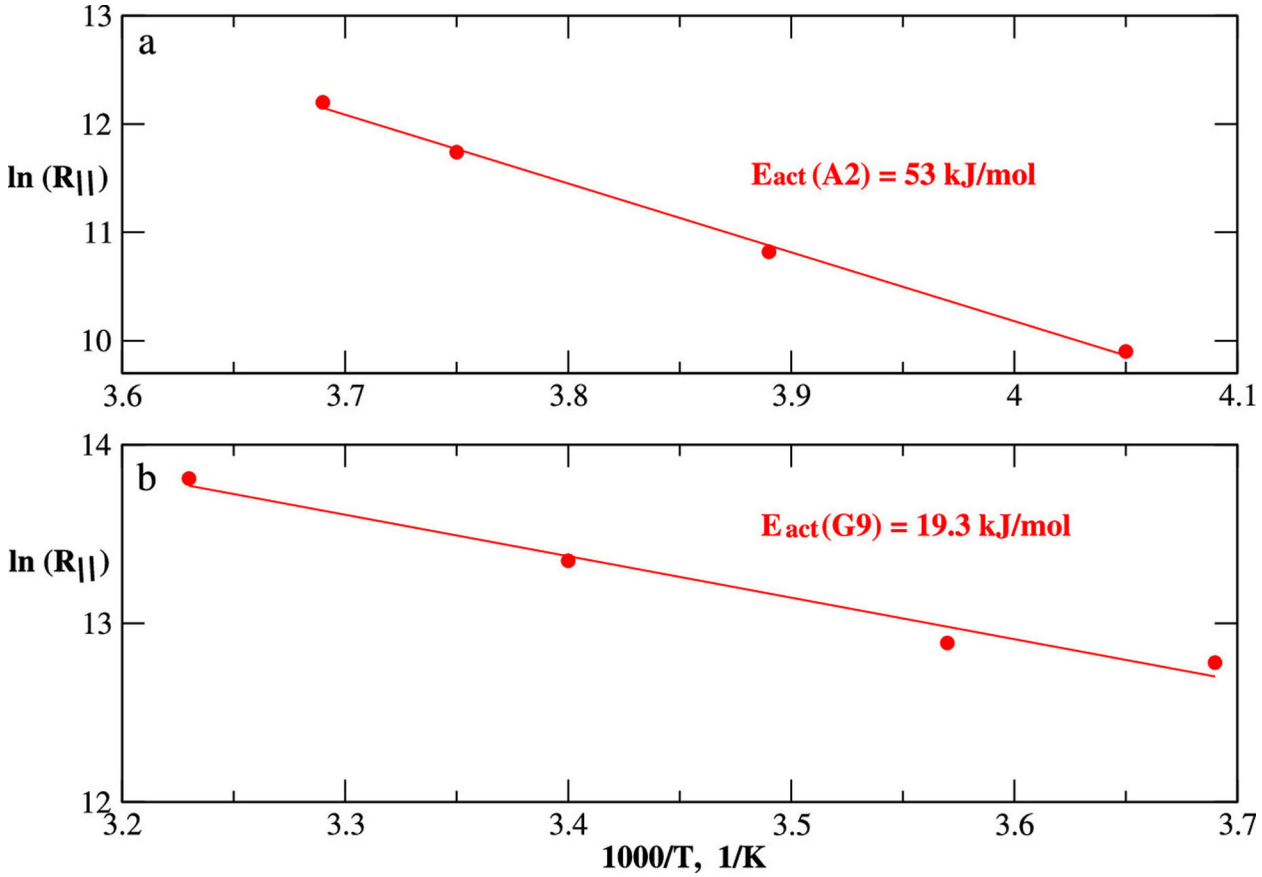

Figure 7.

Natural logarithm of the diffusion rate constant, $R_{\|}$ (given in s^{-1}) as a function of inverse temperature within the scope of the Arrhenius equation for (a) the C^{α}–$C^{\beta}D_3$ probe of residue A2, and (b) the C^{α}–D probe of the residue G9.

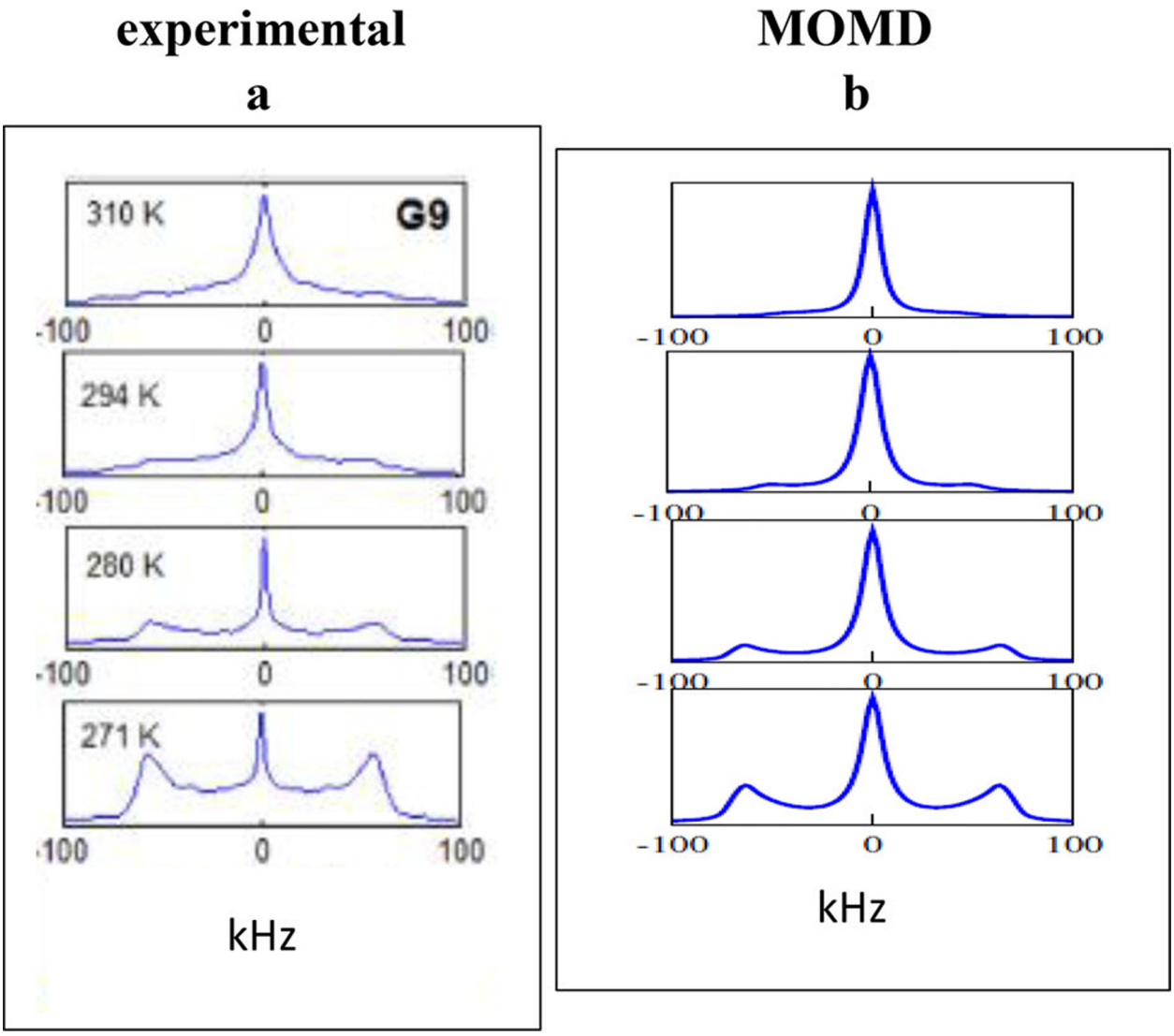

Figure 8.

(a) Experimental ^{2}H spectra of the C$^{\alpha}$–D probe of residue G9 at the temperatures depicted in the figure. Reproduced with permission from Au, D. F.; Ostrovsky, D.; Fu, R.; Vugmeyster, L. Solid-State NMR Reveals a Comprehensive View of the Dynamics of the Flexible Disordered N-Terminal Domain of Amyloid-β Fibrils. *J. Biol. Chem.* **2019**, *294*, 5840–5853. Copyright 2019 of the American Society for Biochemistry and Molecular Biology. (b) ^{2}H MOMD spectra that correspond best to the experimental spectra in (a). The MOMD parameters underlying the (b) spectra are given in Table 3.

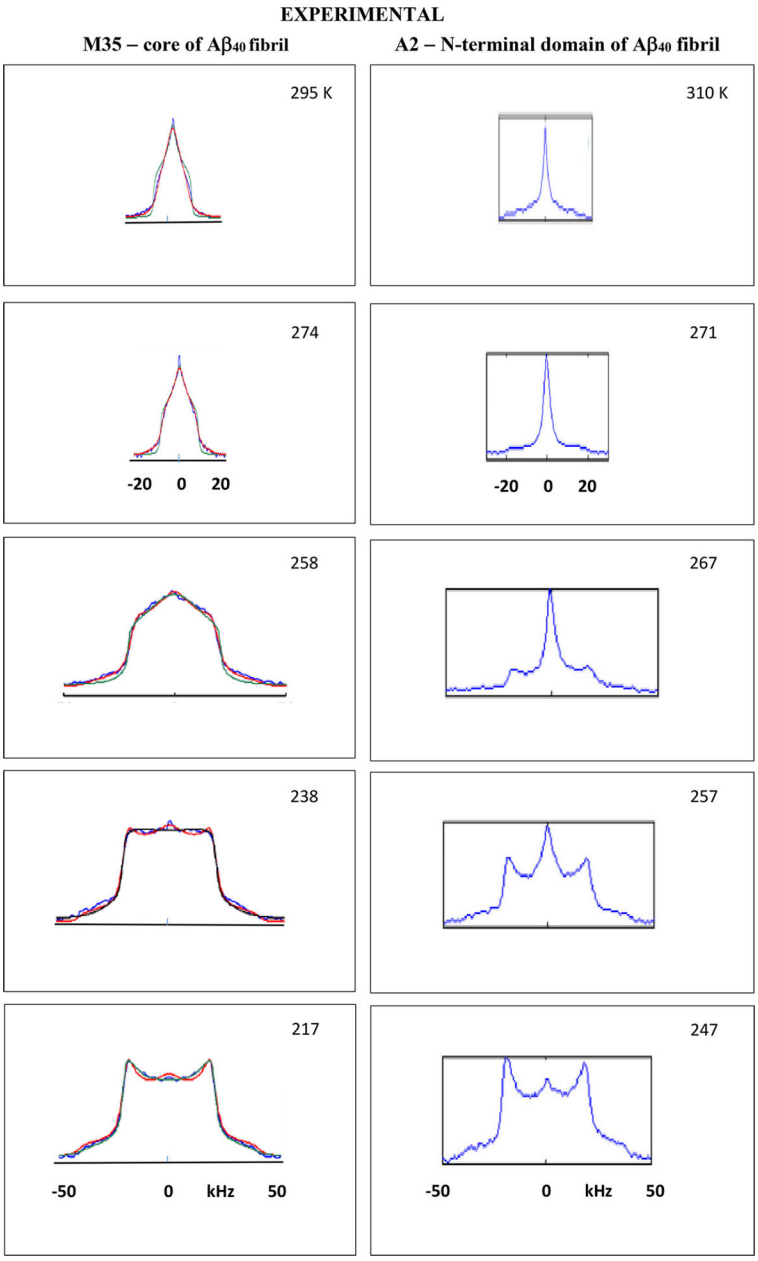

Figure 9.

Evolution with temperature of the experimental ^{2}H spectra of the C^{α}–$C^{\beta}D_3$ probe of residue A2 of the N-terminal domain taken from ref 15 (right). Reproduced with permission from Au, D. F.; Ostrovsky, D.; Fu, R.; Vugmeyster, L. Solid-State NMR Reveals a Comprehensive View of the Dynamics of the Flexible Disordered N-Terminal Domain of Amyloid-β Fibrils. *J. Biol. Chem.* **2019**, *294*, 5840–5853. Copyright 2019 of the American Society for Biochemistry and Molecular Biology. Evolution with temperature of the experimental ^{2}H spectra of the S–$C^{\varepsilon}D_3$ probe of residue M35 of the core domain taken from ref 13 (left).

Table 1.

^{2}H-Labeled Residues of the N-Terminal Domain of the Aβ_{40}-Amyloid Fibril and pertinent probes

residue	**A2**	**F4**	**τ-H 6**	**G9**	**VI2**
probe	C^{α}–$C^{\beta}D_3$	C^{β}–phenyl-d_5	(N-ring)–CD_3	$C^{\alpha}D$	C^{β}–$(C^{\gamma}D_3)_2$

Table 2.

Best-Fit MOMD Parameters Corresponding to the A2 Spectra of Figure 6b Which Reproduce the Experimental Spectra of Figure 6a[a]

T, K	c_0^2	c_2^2	c_0^4	c_2^4	$R_\perp$, s^{-1}	$R_\parallel$, s^{-1}
310	1.0	0.0	1.0	0.0	5.0×10^3	5.0×10^5
271	1.1	1.2	0.5	−0.9	1.6×10^2	2.0×10^5
267	1.3	1.6	0.7	−1.3	1.6×10^2	1.3×10^5
257	1.5	2.0	0.9	−1.7	1.6×10^2	5.0×10^4
247	1.7	2.5	0.9	−1.7	1.6×10^2	2.0×10^4

[a]The best-fit diffusion tilt is $\beta_{MQ} = 58°$.

Table 3.

MOMD Parameters That Generated the Best Agreement with the G9 Spectra of Figure 8b[a]

T, K	c_0^2	c_2^2	c_0^4	c_2^4	$R_\perp$, s^{-1}	$R_\parallel$, s^{-1}
310	1.1	1.4	0.5	−1.1	4.0×10^2	1.0×10^6
294	1.2	1.6	0.5	−1.2	3.2×10^2	6.3×10^5
280	2.0	2.3	2.5	−2.5	1.6×10^2	4.0×10^5
271	2.7	2.5	2.5	−2.5	1.6×10^2	3.2×10^5

[a]The best-fit diffusion tilt is $\beta_{MQ} = 54°$.

Table 4.

Best-fit MOMD Parameters Corresponding to the ^{2}H Spectrum of A2 of the N-Terminal Domain Obtained at 257 K (Figure 6b) and the ^{2}H Spectrum of M35 of the Core Domain Obtained at 258 K (Reference 19)

res; domain	T, K	c_0^2	c_2^2	c_0^4	c_2^4	$\log R_\perp$	$\log R_\parallel$	β_{MQ}°
A2: N-terminal	257	1.5	2.0	0.9	−1.7	2.2	4.7	58
M35; core	258	1.9	2.3	0.0	0.0	2.2	4.3	65